Effective Transport Properties of LiMn$_2$O$_4$ Electrode via Particle-Scale Modeling

Amit Gupta,[a,*,z] **Jeong Hun Seo,**[b] **Xiangchun Zhang,**[b,**] **Wenbo Du,**[a] **Ann Marie Sastry,**[b] **and Wei Shyy**[a,c]

[a]*Department of Aerospace Engineering, and* [b]*Department of Mechanical Engineering, University of Michigan, Ann Arbor, Michigan 48109, USA*
[c]*Department of Mechanical Engineering, The Hong Kong University of Science and Technology, Clear Water Bay, Kowloon, Hong Kong*

The extension of Li-ion batteries, from portable electronics to hybrid and electric vehicles, is significant. Developing a better understanding of the role of material properties and manipulating the morphology of the particle clusters comprising Li-ion electrodes could lead to potential opportunities for attaining higher performance goals, for which the effect of both material properties and morphology needs to be considered in a physics-based model. In this work, different particle packing arrangements are analyzed for the calculation of effective transport properties and reaction density that appear in the porous-electrode formulation due to the volume-averaging process. Surrogate-based analysis is used to systematically construct and validate reduced-order models for species transport at the particle-electrolyte interface. The low effective solid transport predicted through microscale modeling indicates the effect of packing arrangement and tortuosity, an aspect not captured by the Bruggeman's relation. Particle cluster simulations reveal a Li-ion flux quantitatively different than that predicted by the porous-electrode model due to the variation of overpotential at the microscale. The present study offers a first-step towards integration of the effect of microstructure into a macroscale simulation.
© 2011 The Electrochemical Society. [DOI: 10.1149/1.3560441] All rights reserved.

The extension of Li-ion batteries, from portable electronics to hybrid and electric vehicles, is significant. Typically, optimizing the design and performance of a battery-pack begins from the material to the cell level. However, this process can be expensive, both in time and monetary terms, since a design that may be optimum at the cell level may not be the best choice at the pack-scale. In addition, battery performance is directly related to the selection of chemistry, topology of the electrodes, and their tortuosity.

At the battery-scale, the number of variables governing performance increases enormously and can only be analyzed at a reasonable cost in an appropriate mathematical framework. Recent work has shown that performance of Li-ion technology can be improved through emphasis on engineering the microstructural architecture of the electrodes. In such a scenario, developing a better understanding of the role of material properties and manipulating the morphology of the particle clusters comprising Li-ion electrodes could potentially lead to attainment of higher performance goals.

Interrogation of cell performance can be achieved through either experimental or numerical investigations.[1–28] However, numerical simulations provide an advantage over their experimental counterparts since they are able to quantify the effects of several variables in a systematic fashion. As a result, the past two decades has seen a steady incline in the modeling of Li-ion cells. These analyses have separately utilized the equivalent circuit models,[7,8] single-particle model,[9,10] porous-electrode formulation,[11–13] capacity-fade models[14] and microscopic simulations.[15–22] While such analyses have proved successful in predicting the performance of Li-ion cells, further improvements are needed to make them comprehensive. Equivalent circuit models offer rapid prediction of performance as they employ a simplified representation of the cell; however, they do not take into consideration the architecture and physiochemical processes that occur inside the cell.[22] The single-particle model considers the electrode to be a lumped mass, without any consideration of the packing of particles. The porous-electrode models, although they employ a homogenized representation of the two electrodes, do not take into account the spatial variation in the microstructure and local interactions between the solid and electrolyte phases. Another limitation of the porous-electrode formulation is the use of empirical models, such as Bruggeman's equation, which relates the intrinsic

property and porosity with the effective quantity; such an empirical model does not take the electrode architecture into consideration.

To analyze the cell behavior in a holistic sense, the effect of both material properties and morphology need to be considered in a physics-based model. However, constructing a simulation based on such disparate length scales would be computationally intensive and may be infeasible given the computational capability of present-day computers. A possible solution is to combine the processes that occur at the discharge and electrochemical time scales by including the microstructure into a porous-electrode based formulation, which will assist in borrowing the positive features of both formulations.

Microscopic simulations directed towards multiscale modeling of battery electrodes have previously been successfully demonstrated.[16–22] Through particle-scale modeling of ellipsoidal particles, it has been shown that larger particles and higher discharge rates lead to higher intercalation-induced stresses in LiMn$_2$O$_4$ electrodes.[16] In a separate study, it was shown that heat generation increases with an increase in particle size and potential sweep rate.[17] Using a two-dimensional simulation, the effect of electrode morphology on achievable power has been investigated through microscopic modeling.[18] It was shown that a small, well-dispersed particle distribution resulted in higher active material utilization and higher power density. The role of particle size, shape, morphology and packaging on cell performance has been investigated through numerical simulations on experimentally obtained electrode microstructures.[20] However, these aforementioned analyses have been limited to single particle[16,17] or two-dimensional[18,20] simulations. In a separate study, employing interpenetrating tortuous and ordered branches in electrodes was shown to outperform the conventional rocking-chair configuration using finite-element simulations.[21] Although conceptually attractive, these designs provide added complexity in manufacturing and a higher likelihood of internal short-circuit upon fast charging. Clearly, significant milestones are yet to be achieved before the microstructure can be integrated into a cell-level simulation.

In this work, we aim to extend multiscale modeling efforts[22] by analyzing the electrochemical processes at the particle-scale in the cathode of a Li-ion cell. Several electrode microstructures, constructed based on randomly packed ellipsoidal particles, have been simulated to calculate effective transport properties, such as diffusivity and electronic conductivity, and reaction density for incorporation into cell-based simulations. Volume averaging[23–25] has been used to capture the physics on multiple scales. Since microscopic

* Electrochemical Society Student Member.
** Electrochemical Society Active Member.
z E-mail: amitgupt@umich.edu

models to analyze a LiMn$_2$O$_4$ electrode are accurate but computationally expensive, and macroscopic models are simplified but efficient, volume averaging can be used as a bridge between the two alternatives. Thus, our objectives in this work are as follows:

1. Develop the volume-averaged equations starting from the microscopic species conservation for both Li-ion and charge in the solid and the electrolyte and demonstrate the form of the closure terms that appear in the cell-level simulation.

2. Introduce surrogate-based analysis to conduct three-dimensional numerical experiments on randomly arranged ellipsoidal particles in a representative elementary volume (REV) to capture the physics at the microscale using the boundary conditions based on a macroscopic simulation.

3. Calculate the effective transport properties and reaction density at the particle-electrolyte interface and construct reduced-order models using surrogate analysis for the latter using simulations of multiple particle clusters.

4. Conduct sensitivity analysis to ascertain the dependence of the reaction density on the solid and electrolyte concentrations, potentials, and concentration and potential gradients.

Methodology

In Li-ion cells, the discharge and electrochemical insertion/removal processes occur at scales that are different by orders of magnitude.[22] To successfully model the physics of a cell, a framework that could capture these disparate scales is required. This is only possible if the selected grid resolution can at least capture the microscale reactions occurring at the particle-electrolyte interface. However, such direct simulation would be impractical, as present day computers do not have the power and capability to handle a mesh that may consist of O(10^{10}) discrete points based on resolving every single particle in the electrode.[22] An alternative approach is to develop a micro-macro model by creating an intermediate scale which may represent the physics when scales much smaller than the computational mesh are employed. One such option is to include the effect of the microstructure in a macroscopic model through the volume averaging technique. This technique has been used effectively in modeling multiphase flows[26] and transport in porous media.[27]

In this work, the microscopic behavior of a Li-ion electrode has been simulated using the following microscale governing equations.

Microscale Governing Equations

The particle-electrolyte system, enclosed in a representative volume, is simulated using Eqs. 1–4 that govern the variation of Li-ion concentration and the electric potential in the two phases[23–25]

$$\frac{\partial c_s}{\partial t} + \nabla \bullet (-D_s \nabla c_s) = 0 \qquad [1]$$

$$\frac{\partial c_e}{\partial t} + \nabla \bullet (-D_e \nabla c_e) + \frac{\vec{i}_e \bullet \nabla t_+^0}{F} = 0 \qquad [2]$$

$$\nabla \bullet (\sigma \nabla \varphi_s) = 0 \qquad [3]$$

$$\nabla \bullet \left(-\kappa \nabla \varphi_e - \frac{\kappa RT}{F} \left(1 + \frac{\partial \ln f}{\partial \ln c_e} \right) \left(1 - t_+^0 \right) \nabla \ln c_e \right) = 0 \qquad [4]$$

In Eq. 4, f is the mean molar activity coefficient of electrolyte, which is typically assumed to be a constant due to lack of data. As a result, Eq. 4 can be simplified to

$$\nabla \bullet (\kappa \nabla \varphi_e + \kappa_D \nabla (\ln c_e)) = 0 \qquad [5]$$

where $\kappa_D = \kappa RT/F \left(1 + \partial \ln f / \partial \ln c_e \right) \left(1 - t_+^0 \right)$.

The governing equations at the microscale (i.e., Eqs. 1–5) can be volume-averaged[26,27] to obtain the porous-electrode form of the macroscale governing equations.[24,25] The volume-averaged porous-electrode pseudo-2D model[11,12] uses a microstructure that is composed of a single spherical particle placed at each grid location in the electrode. As a result, it cannot account for the percolation networks in particle clusters. Moreover, pseudo-2D models do not solve for the electric potential variation in the microstructure. Therefore, the focus in the present work is on the application of microscale equations to particle aggregate-electrolyte composite to capture percolating particle networks and the variation of concentration and electric potential at the microscale, and eventually to couple these features with a macroscale simulation via surrogate modeling.[29,34–36]

Basic concepts and theorems that assist in transforming the microscopic to the macroscopic governing equations are illustrated in Appendix A.

Volume-Averaged Li-ion and Charge Transport in Solid Particles

As a precursor to the volume averaging approach, we focus on the transformation of the equation describing the diffusion of Li-ions and charge transport in the solid phase of the electrode. Equation 1 when multiplied by γ_s can be integrated to give

$$\frac{1}{dV} \int_{dV} \gamma_s \frac{\partial c_s}{\partial t} dV = \frac{1}{dV} \int_{dV} \gamma_s \nabla \bullet (D_s \nabla c_s) dV \qquad [6]$$

From Theorem 1 (Eq. A.6 in Appendix A), the integral on the left can be written as

$$\frac{1}{dV} \int_{dV} \gamma_s \frac{\partial c_s}{\partial t} dV = \frac{\partial}{\partial t} \left[\frac{1}{dV} \int_{dV} \gamma_s c_s dV \right] - \frac{1}{dV} \int_{dA_s} c_s \vec{w} \bullet \vec{n} dA$$

$$= \frac{\partial \overline{c_s}}{\partial t} - \frac{1}{dV} \int_{dA_s} c_s \vec{w} \bullet \vec{n} dA \qquad [7]$$

From Theorem 2 (Eq. A.7 in Appendix A), the integral on the right reduces to

$$\frac{1}{dV} \int_{dV} \gamma_s \nabla \bullet (D_s \nabla c_s) dV = \nabla \bullet \left[\frac{1}{dV} \int_{dV} (D_s \nabla c_s) \gamma_s dV \right]$$

$$+ \frac{1}{dV} \int_{dA_s} (D_s \nabla c_s) \bullet \vec{n} dA$$

$$= \nabla \bullet \overline{(D_s \nabla c_s)} + \frac{1}{dV} \int_{dA_s} (D_s \nabla c_s) \bullet \vec{n} dA \qquad [8]$$

Putting the two sides together

$$\frac{\partial \overline{c_s}}{\partial t} - \frac{1}{dV} \int_{dA_s} c_s \vec{w} \bullet \vec{n} dA = \nabla \bullet \overline{(D_s \nabla c_s)} + \frac{1}{dV} \int_{dA_s} (D_s \nabla c_s) \bullet \vec{n} dA \qquad [9]$$

Since the movement of the solid–electrolyte interface in a Li-ion cell can be assumed to be negligible, $\int_{dA_s} c_s \vec{w} \bullet \vec{n} \, dA = 0$. Therefore

$$\frac{\partial \overline{c_s}}{\partial t} = \nabla \bullet \overline{(D_s \nabla c_s)} + \frac{1}{dV} \int_{dA_s} (D_s \nabla c_s) \bullet \vec{n} dA \qquad [10]$$

where $\overline{(D_s \nabla c_s)}$ and $\frac{1}{dV} \int_{dA_s} (D_s \nabla c_s) \bullet \vec{n} dA$ are the closure terms which require special treatment. In a similar fashion, the microscopic transport equation for charge in the solid phase (Eq. 3) can be simplified using the volume averaging approach to the following

$$\nabla \bullet \overline{(\sigma \nabla \varphi_s)} + \frac{1}{dV} \int_{dA_s} (\sigma \nabla \varphi_s) \bullet \vec{n} dA = 0 \qquad [11]$$

Conventionally, the volume-averaged species flux is modeled based on the effective material properties. For example

$$\overline{(D_s \nabla c_s)} = D_s^{eff} \nabla \overline{c_s} \qquad [12a]$$

$$\overline{(\sigma \nabla \varphi_s)} = \sigma_{eff} \nabla \overline{\varphi_s} \qquad [12b]$$

where

$$D_s^{eff} = D_s \varepsilon_s^{\alpha} \qquad [13]$$

In the porous-electrode theory, α is typically assumed to be given by the Bruggeman's exponent (i.e., $\alpha = 1.5$). Fuller et al.[12] and Patel et al.[28] have observed that for real electrodes and separators, the exponent varies significantly from 1.5. The former used an exponent of 4.5 to model electronic conductivity that matched with experimental measurements, whereas the latter reported that the exponent varied between 2.8 and 10.4 for microporous separators. In addition, pseudo-2D models[11–13] that are based on the porous-electrode theory solve the volume-averaged species and charge conservation equations in the electrolyte; however, the species transport equation in the solid is solved based on the intrinsic diffusion coefficient (i.e., using Eq. 1). For the volume-averaging process to be applicable at each grid location in the electrode, the estimation of effective diffusivity and conductivity in both particle and electrolyte phases is essential.

The second closure term on the right hand side of Eq. 10 can be written as

$$J_{C_s} = \frac{1}{dV} \int_{dA_s} (D_s \nabla c_s) \cdot \vec{n} dA \qquad [14]$$

and is known as the volumetric flux density. This integral has traditionally been modeled in pseudo-2D simulations as the product of interfacial specific area and a mean interfacial flux[11,12,24] through

$$J_{C_s} = a_s j_{flux} \simeq \frac{3\varepsilon_s}{R_s} j_{flux} \qquad [15]$$

where

$$j_{flux} = k c_e^{0.5} (c_t - c_s)^{0.5} c_s^{0.5} \left[\exp\left(\frac{F}{2RT}\eta\right) - \exp\left(-\frac{F}{2RT}\eta\right) \right] \qquad [16]$$

is the reaction flux per unit area computed from the Butler-Volmer equation based on local Li-ion concentration in the solid, volume-averaged Li-ion concentration in the liquid and volume-averaged electric potentials in the solid and electrolyte phases. In addition, the overpotential is given by

$$\eta = \varphi_s - \varphi_e - U_{OCP} \qquad [17]$$

A more accurate approach to calculate the volumetric flux is to use the local values of the variables and perform surface integration of the local flux at the particle-electrolyte interface using Eq. 14.[23,25] The computed reaction density can then be used to construct reduced-order models which in turn can be readily integrated into a macroscopic simulation. To achieve this crucial step, surrogate tools have been uniquely adopted to identify the reduced-order relationships between microscopic simulations and the closure terms of the volume-averaged equations.

Surrogate Modeling and Analysis

Surrogate modeling is concerned with the determination of a continuous function of a set of independent variables from a limited amount of data.[29] In other words, it can be employed to correlate design variables of a mathematical or experimental set-up with the outcomes (or objective functions) of the design process. The surro-

gate models constructed in such a manner can be used for fast prediction and evaluation of the design problem. In the multiscale modeling framework, surrogate models constructed on numerical simulations used to calculate the closure terms and effective transport properties provide an opportunity to combine the physics at various scales in a computationally efficient manner.

The surrogate modeling process begins by constructing a set of experiments known as design of experiments (DOE) at selected points in design space. The simplest way to select these points is to use random sampling; however, such a method may require a large number of points to avoid any particular bias in the design space. Latin hypercube sampling (LHS) is an improvement, since it ensures a stratified sample within the full range of the sample space.[29] However, LHS cannot ensure sampling at the extrema of the variables. As a result, face centered composite design (FCCD) is also used to sample the face-center and vertices of the design hypercube.

Results

In this work, we intend to calculate the closure terms and effective material properties that appear in the volume-averaged equations using microscopic scale simulations based on a cluster of particles enclosed in an REV. The solid phase was assumed to be composed of 10 $LiMn_2O_4$ ellipsoidal particles of aspect ratio 2. The volume fraction of the initial solid phase packing was held at 0.6. These uniform-sized particles were arranged using a molecular dynamics based packing algorithm[30] for an initial volume fraction of the solid phase of 0.6, such that they contacted each other at the boundary. Thereafter, to create an overlapping region and thus a conduction path for the transport of electrons inside the solid, the size of the ellipsoidal particles was increased along the major and minor axes by a factor of 1.1. The particle cluster was discretized using uniform sized cubic voxels,[15,31,32] a method commonly adopted for finite-element analysis of complex structures. The portion of the solid that remained outside a 10 μm cubic domain was removed. The equivalent particle size that occupies the same volume in a 10 × 10 × 10 μm domain would be 5.23 μm. The void space surrounding the particle cluster was prescribed as the electrolyte phase, chosen to be $LiPF_6$ in EC:DMC (a mixture of ethylene carbonate and dimethyl carbonate).

The governing equations were solved using the finite-element based solver COMSOL. A total of 24 random realizations were generated to statistically average the effective properties and reaction density closure terms that appear in the macroscopic equations. The material properties used for the solid and electrolyte phases are given in Tables I and II respectively. To check for grid independence of results, a selected microstructure at different mesh resolutions was simulated. The generalized minimal residual (GMRES) solver with the symmetric successive over-relaxation (SSOR) preconditioning method[33] was used to solve the discretized equations. Lagrange-quadratic elements were used for interpolation. With a sample mesh spacing of 0.5 μm (i.e., 9261 voxel elements), approximately 4 to 6 GB of memory (on an Intel 7 desktop) was required in simulating each sampling point of the design of experiments. The

Table I. Material properties for $LiMn_2O_4$.

Property	Expression
D_s	$10^{-13} \mathrm{m^2/s}$
σ	3.8 S/m
c_t	23634 mol/m3
y	c_s/c_t
U_{ocp}	$4.06279 + 0.0677504 \tanh(-21.8502y + 12.8268)$
	$-0.105734 \left[(1.00167 - y)^{-0.379571} - 1.575994 \right]$
	$-0.045 e^{-71.69y^8} + 0.01 e^{-200(y-0.19)} \mathrm{V}$
k	$3 \times 10^{-11} \mathrm{mol^{-1/2} m^{5/2}/s}$

Table II. Material properties for LiPF$_6$ in EC:DMC.

Property	Expression
D_e	$5.34 \times 10^{-10} e^{-0.65 c_e 1000} \mathrm{m^2/s}$
κ	$0.0911 + 1.9101\left(\frac{c_e}{1000}\right) - 1.052\left(\frac{c_e}{1000}\right)^2 + 0.1554\left(\frac{c_e}{1000}\right)^3 \mathrm{S/m}$

variation of surface integrated reaction density with increasing number of voxel elements (and decreasing mesh spacing) is shown in Fig. 1. A sample simulation with the two resolutions of 0.5 and 0.2 μm took about 3 and 43 min respectively, with the maximum difference in computations observed to be 5.99%. As part of the construction of surrogate models, approximately 10^4 simulations were conducted, which took 21 days of CPU time with a mesh resolution of 0.5 μm. Any further increase in the resolution (i.e., decrease in mesh spacing) would have increased the CPU time by at least a factor of two. Since the gain in accuracy with an increase in resolution is not significant as compared to increase in computational time, a grid resolution of 0.5 μm was adopted for computing the closure terms, namely the effective transport properties and reaction density, of the volume-averaged equations.

Effective Transport Properties

We first begin by calculating the effective transport properties that appear in Eq. 12 as a result of the volume-averaging process. The ratio of the effective transport to the bulk property carries the same value (i.e., D_s^{eff} and σ_s^{eff} for the solid phase and D_e^{eff}, κ^{eff} and κ_D^{eff} for the electrolyte) since they share the same functional relationship with the corresponding bulk properties (see, for example, Eq. 12). For simplicity, only the results for the calculation of effective diffusivity for the solid and electrolyte are presented.

To calculate the ratio given by D_k^{eff}/D_k where $(k = s, e)$, the 3D particle realizations were packed in a $1 \times 1 \times 1$ m cubic domain, and the steady-state diffusion equation given by

$$\nabla \cdot (D \nabla c) = 0 \qquad [18]$$

was solved with concentration boundary conditions imposed at the top $(c = 1 \text{ mol/m}^3)$ and bottom $(c = 0 \text{ mol/m}^3)$ and with symmetry for the other boundaries. For reference, the bulk diffusion coefficient was defined as $D = 1 \text{ m}^2/\text{s}$. From the steady-state concentration profile in the solid, the effective diffusivity D^{eff} was computed through Eq. 12a as
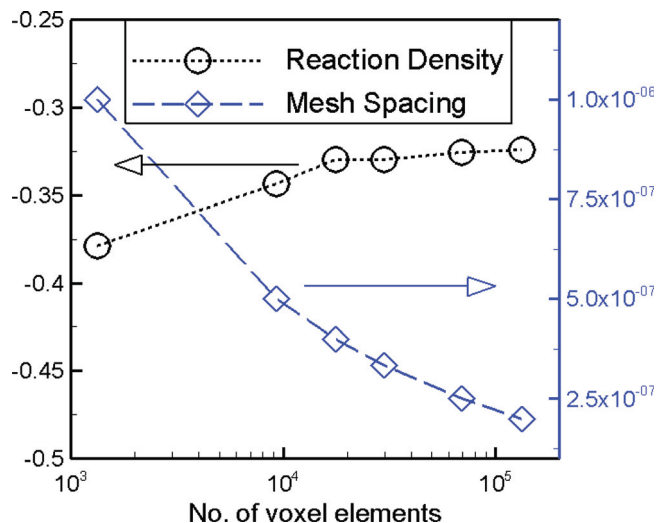

Figure 1. (Color online) Reaction density (in A/m^2) computed for increasing number of voxel elements and different mesh spacings (in m) for a sample simulation.

$$\frac{D^{eff}}{D} = \frac{\left[\int_A \nabla c\, dA\right]\Big|_{z=L}}{A_s[c(z=L) - c(z=0)]/L} \qquad [19]$$

where $A_s = 1 \text{ m}^2$ and $L = 1 \text{ m}$.

For the 24 particle realizations analyzed in this work, Eq. 19 was used to compute the ratio of the effective and bulk diffusivity for both the solid and electrolyte phases. Table III summarizes the results for the average ratio and the standard deviation recorded in the numerical simulations. Steady state concentration profiles for the maximum and minimum effective solid diffusion coefficients observed in the simulations are also shown in Fig. 2.

Surrogate Analysis for Reaction Density

To bridge the gap between microscopic simulations of particle clusters and cell-level simulations and estimation of volume-averaging closure terms, Li-ion concentration, electric potential and their gradients in the solid and electrolyte phase were chosen as design variables for formulating reduced-order models using surrogate-based analysis. The range of these eight design variables, as shown in Table IV, were chosen to cover the range of values that appear in a macroscopic simulation using the pseudo-2D formulation.[11,12] The Li-ion concentration was normalized with the theoretical maximum so that it may be represented in terms of instantaneous state of charge (SOC) at any location in the electrode. The ranges were determined based on a maximum possible discharge rate of 3C. This range of design variables was used to construct a preliminary DOE consisting of points selected based on filling the design space using FCCD and LHS. However, to avoid numerical instability issues, arising due to the exponential terms in the Butler-Volmer equation, the initial DOE was filtered through the condition $-0.1 \leq \overline{\varphi}_s - \overline{\varphi}_e - U_{OCP}(\overline{\tilde{c}}_s) \leq 0$ to a reduced DOE which consisted of 12 FCCD and 375 LHS points. Numerical simulations were run on these sample points for further analysis, including construction of reduced-order surrogate models. For cross-validation of these surrogate models, 16 additional test points were created using LHS so as to reduce their correlation with the original DOE. To further estimate the accuracy of surrogate models, a parameter called the prediction error sum of squares (PRESS) was also computed. PRESS quantifies the error in the construction of surrogate models based on existing data and is computed from the training points of the DOE using the leave-one-out strategy. The root-mean-square PRESS was computed directly from the training data by summing the prediction errors at all data points[13,29] through the following equation

$$PRESS_{RMS} = \sqrt{\frac{1}{N_s} \sum_{i=1}^{N_s} \left(y_i - \hat{y}_i^{(-i)}\right)^2} \qquad [20]$$

where N_s is the number of sampling points, y_i is the prediction of the surrogate model at $\mathbf{x}_i$, and $\hat{y}_i^{(-i)}$ respresents the prediction at $\mathbf{x}_i$ using the surrogate constructed using all sample points except $\mathbf{x}_i$.[13,29] Although expensive to compute for a large number of training points,

Table III. Computed ratios of the effective to bulk transport properties averaged over 24 microstructures using 3D microscale simulations compared with the Bruggeman's equation for the solid and electrolyte phases. The solid volume fraction is 0.6.

	Microscale simulations (D_k^{eff}/D_k)		Bruggeman's equation
	Mean	Standard deviation	
Solid	0.267	0.068	0.465
Electrolyte	0.273	0.041	0.253
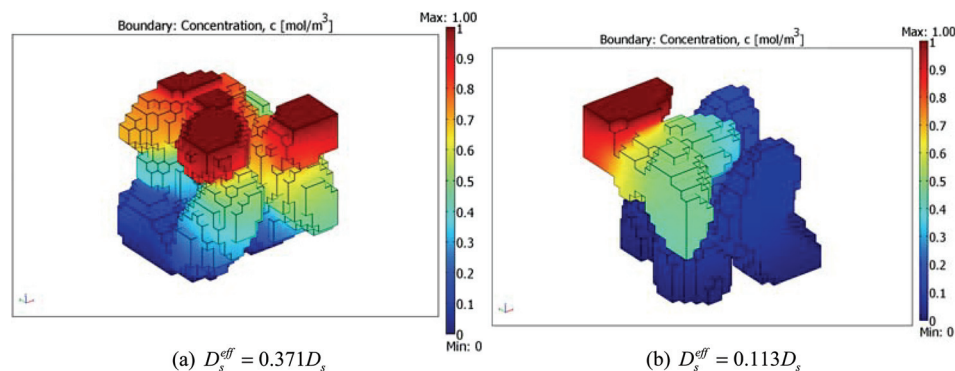
Figure 2. (Color online) Concentration profiles in two contrasting cases for effective property calculation.

(a) $D_s^{eff} = 0.371 D_s$ (b) $D_s^{eff} = 0.113 D_s$

PRESS offers quality assessment for best model selection when many alternatives are available.

In the current microscopic simulations, each point of the DOE identifies the local values of the design variables at a given node on the macroscopic mesh of a Li-ion positive electrode. To simulate the microstructure based on macroscopic variation of concentration and electric potential, boundary conditions as shown in Fig. 3 were enforced. For the solid phase, constant concentration and potential boundary conditions were imposed at the planes corresponding to $z = 0$ and $z = L$. For instance, for the solid at $z = L$, $c(z = L) = \overline{\overline{c}}_s + L/2 \times \partial \overline{\overline{c}}_s / \partial z$, where $\overline{\overline{c}}_s$ and $\partial \overline{\overline{c}}_s / \partial z$ are based on the sampling point of the DOE. The four other boundary planes (x–z and y–z) were prescribed as symmetric and insulated. A similar procedure was also adopted for the electrolyte phase. At the interface between the solid and the electrolyte, flux based on the Butler-Volmer reaction current was enforced such that the net flux between the two phases was zero. The concentrations and electric potentials in the solid and electrolyte were initialized to the values corresponding to those obtained through the DOE. Steady-state simulations, using Eqs. 1–3 and 5 were conducted to calculate the variation of concentration and the electric potential in the particle-electrolyte domain. The DOE (consisting of 387 sample points) was simulated for each of the 24 different particle arrangements, and the reaction density at the particle-electrolyte interface recorded. A mean value of the normalized reaction density was considered for surrogate analysis.

Several different models were trained on the sample points, including polynomial response surface (PRS), kriging (KRG) and radial-basis neural network (RBNN). Details on the form of each of these models are described in Appendix B. The current design of experiments contained a sufficient number of data points to fit at most a 3rd order polynomial surface. Attempts to fit higher-order PRS yielded poor results due to an inadequate number of data points. For kriging, both first- and second-order polynomial regression models were considered with the Gaussian and cubic spline correlation functions. The best kriging model was obtained by using only the maximum test point prediction error as the optimization criterion and ignoring the RMS error to minimize prediction error at the selected test points. As shown in Fig. 4, for a second-order poly-nomial regression and Gaussian correlation model, the prediction errors at test points were greatly reduced. Additionally, PRESS$_{RMS}$ values were also significantly reduced with the optimized kriging model. To construct the RBNN models, a total of 100 neurons were used in all cases. An optimized spread coefficient value of 3.683 was found to maximize the adjusted coefficient of determination. While this optimized RBNN model performed better, it could not match the quality of fit of the optimized kriging model.

Based on the second-order regression with Gaussian correlation kriging model, global sensitivity analysis was conducted to understand the importance of concentrations, electric potentials and their gradients on the normalized reaction density calculations. The importance of each of the eight variables is quantified based on main and total indices. The main index represents the influence of a design variable on the objective function when analyzed in isolation; the total index indicates the combined contribution due to any partial variance in which the design variable may be involved.[29] The main and total index for the three main design variables computed from the kriging model with least error measures is shown in Fig. 5. The indices computed for the other variables, namely electrolyte concentration and gradients of concentrations and potentials in both phases, were found to be negligible and thus are not shown.

Comparison of Micro- and Macroscale Models

The predictions from the microscale simulations for different particle clusters were also compared with the pseudo-2D cell model. For the cell model, Carbon was chosen as the negative electrode with electrode thickness, particle size, diffusion coefficient, conductivity and porosity given by $\delta_n = 100 \, \mu m$, $R_{s,n} = 10 \, \mu m$, $D_{s,n} = 3.9 \times 10^{-14} \, m^2/s$, $\kappa_n = 100 \, S/m$ and $\varepsilon_n = 0.4$ respectively. Material properties listed in Table I were used for the LiMn$_2$O$_4$ electrode, including an electrode thickness of $\delta_p = 100 \, \mu m$. The separator was chosen to have a thickness of $\delta_s = 25 \, \mu m$. Cell simulations were run for two discharge rates of C/2 and 1C to record the macroscopic time variation of concentrations and electric potentials in the two phases. The procedure adopted in the calculation of reaction density at three different locations can be described as follows. First, the pseudo-2D model was simulated under galvanostatic conditions. The variation of

Table IV. Design variables and their ranges used in the particle-cluster modeling.

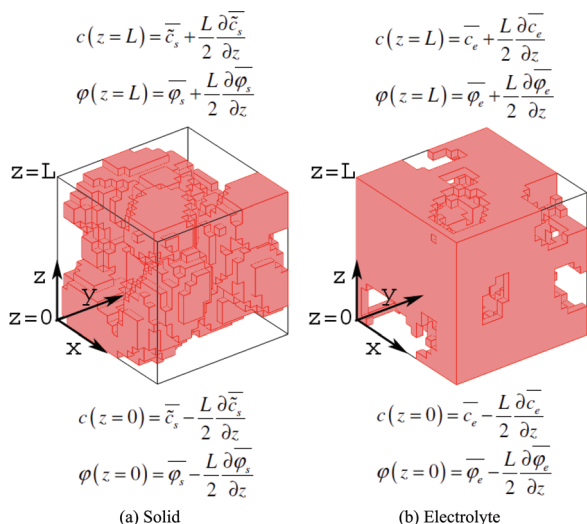| Variables	Minimum value	Maximum value
Li-ion concentration in the solid ($\overline{\overline{c}}_s$)	0.2	0.9
Li-ion concentration in the electrolyte ($\overline{c}_e$)	600 mol/m^3	1000 mol/m^3
Electric potential in the solid ($\overline{\varphi}_s$)	3.0 V	4.15 V
Electric potential in the electrolyte ($\overline{\varphi}_e$)	−1.0 V	0
Li-ion concentration gradient in the solid ($\frac{\partial \overline{\overline{c}}_s}{\partial z}$)	−3500 m^{-1}	0
Li-ion concentration gradient in the electrolyte ($\frac{\partial \overline{c}_e}{\partial z}$)	−6.5 × 10^6 mol/m^4	0
Electric potential gradient in the solid ($\frac{\partial \overline{\varphi}_s}{\partial z}$)	−40 V/m	0
Electric potential gradient in the electrolyte ($\frac{\partial \overline{\varphi}_e}{\partial z}$)	−550 V/m	0

$$c(z = L) = \overline{c}_s + \frac{L}{2}\frac{\partial \overline{c}_s}{\partial z}$$

$$\varphi(z = L) = \overline{\varphi}_s + \frac{L}{2}\frac{\partial \overline{\varphi}_s}{\partial z}$$

$$c(z = 0) = \overline{c}_s - \frac{L}{2}\frac{\partial \overline{c}_s}{\partial z}$$

$$\varphi(z = 0) = \overline{\varphi}_s - \frac{L}{2}\frac{\partial \overline{\varphi}_s}{\partial z}$$

(a) Solid

$$c(z = L) = \overline{c}_e + \frac{L}{2}\frac{\partial \overline{c}_e}{\partial z}$$

$$\varphi(z = L) = \overline{\varphi}_e + \frac{L}{2}\frac{\partial \overline{\varphi}_e}{\partial z}$$

$$c(z = 0) = \overline{c}_e - \frac{L}{2}\frac{\partial \overline{c}_e}{\partial z}$$

$$\varphi(z = 0) = \overline{\varphi}_e - \frac{L}{2}\frac{\partial \overline{\varphi}_e}{\partial z}$$

(b) Electrolyte

Figure 3. (Color online) Voxel representations of the solid and electrolyte phases with the boundary conditions imposed across the two phases for one sample particle cluster arrangement, where $L = 10 \times 10^{-6} m$.

concentration, potentials and their gradients at three different spatial locations at different time instants were recorded. These values were then used to impose concentration and potential boundary conditions across the microstructure (as described earlier), and steady-state computations on the microstructure were then performed. From the steady state profiles, the surface integrated reaction density was retrieved and compared with that predicted by the pseudo-2D formulation. Three unique particle arrangements shown in Fig. 6 were probed to understand the role of particle packing and tortuosity on the prediction of local reaction density. Microstructures 3 and 15 were selected due to their low effective transport. Microstructure 22 was selected since the effective transport from this cluster is similar to the average recorded for the 24 arrangements.

Comparisons for the normalized reaction density were conducted at three different locations in the positive electrode, at locations corresponding to distance of 25, 50 and 75 μm from the separator-positive electrode boundary. Figures 7 and 8 show the variation of normalized reaction density in the micro- and macroscopic simulations as a function of time for discharge rates of 1C and C/2 respectively. The microscale variation of concentration in the solid phase and reaction density at the interface was also analyzed at a location which was fixed at 25 μm from the separator (Fig. 7a). The Li-ion
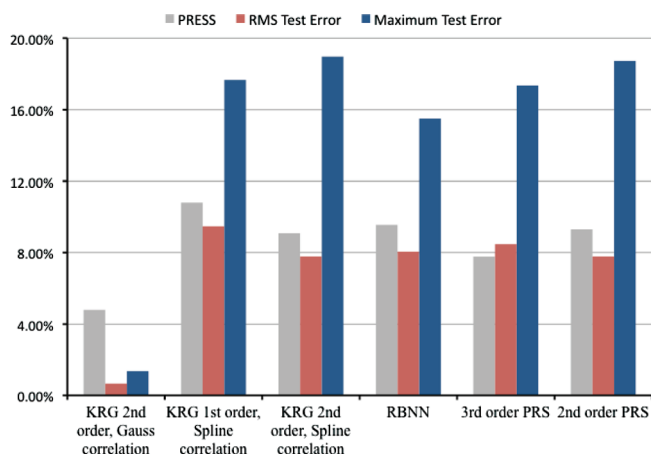

Figure 4. (Color online) Error measures obtained through different surrogate models trained on the design of experiments for prediction of normalized reaction density.
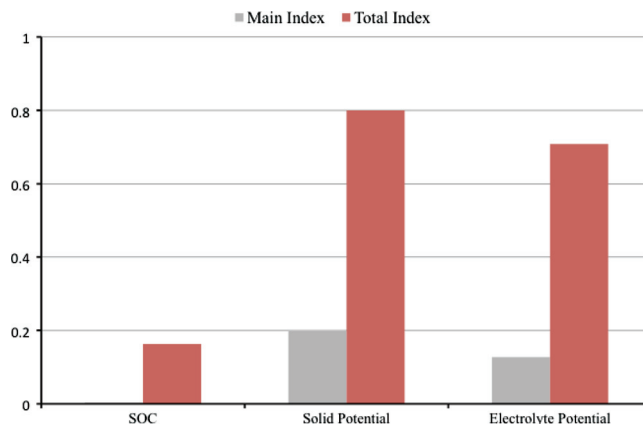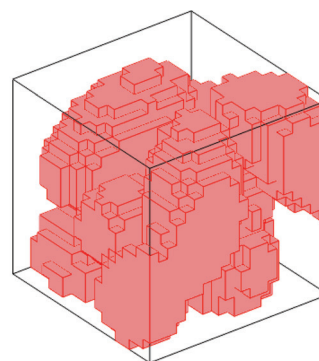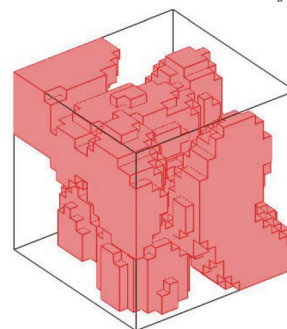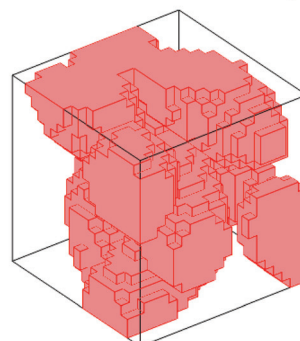

Figure 5. (Color online) Main and total sensitivity indices computed using the kriging model with second-order regression and Gaussian correlation. The indices for the other design variables were negligible, and hence are not shown.

(a) Microstructure 3 with $D^{eff}/D_s = 0.139$

(b) Microstructure 15 with $D^{eff}/D_s = 0.113$

(c) Microstructure 22 with $D^{eff}/D_s = 0.266$

Figure 6. (Color online) Three solid microstructures with different effective diffusivities simulated for comparison with pseudo-2D simulations.
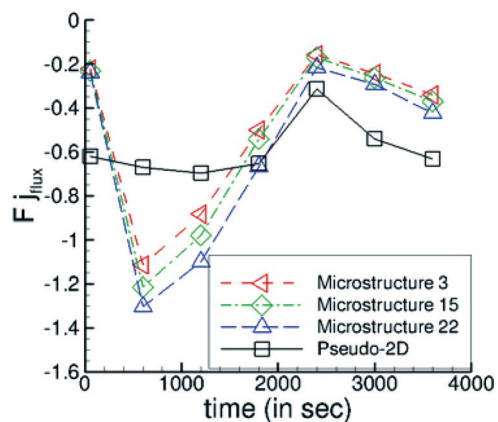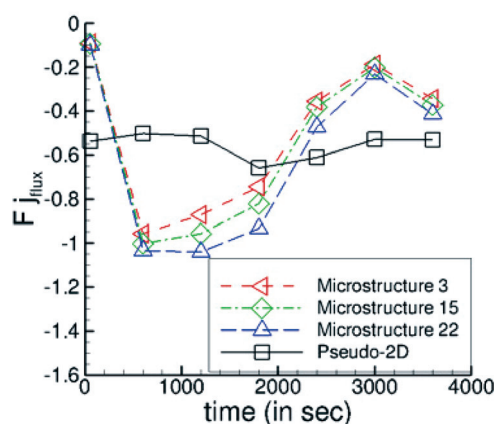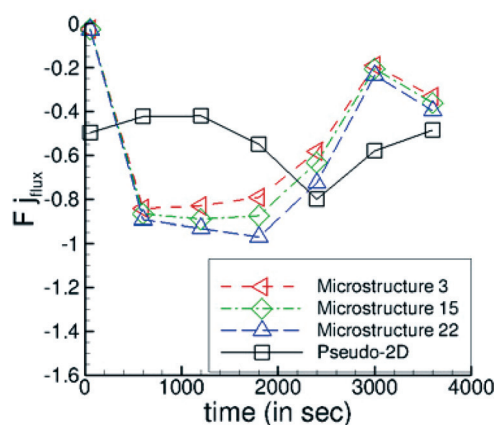
(a) 25 μm from the separator

(b) 50 μm from the separator

(c) 75 μm from the separator

Figure 7. (Color online) Normalized reaction density (in A/m^2) calculated at three different locations in the positive electrode for 1C discharge rate.

(a) 25 μm from the separator

(b) 50 μm from the separator

(c) 75 μm from the separator

Figure 8. (Color online) Normalized reaction density (in A/m^2) calculated at three different locations in the positive electrode for C/2 discharge rate.

concentration (state of charge) in the solid for microstructure 22 for 1C discharge rate at selected time instants is shown in Fig. 9. In addition, the local reaction density for microstructure 22 corresponding to the three time instants is shown in Fig. 10.

Discussion

Based on the calculation of effective transport properties, as shown in Table III, a few observations can be made. First, the effective solid diffusivity calculated through 3D modeling of particle
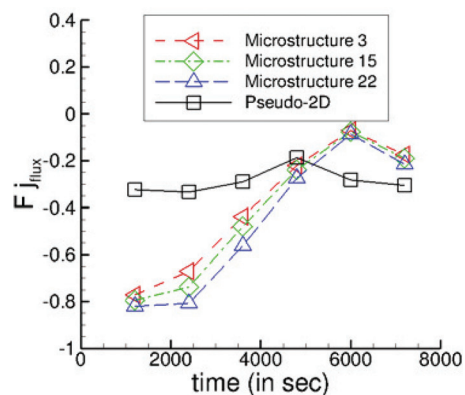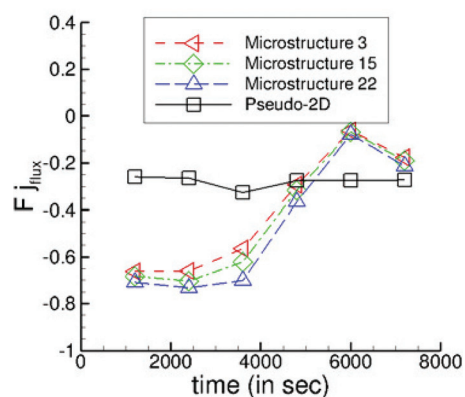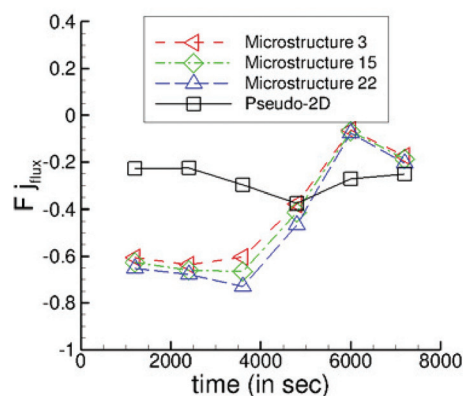
clusters is much lower than that predicted using Bruggeman's equation. Secondly, the average effective diffusivity of the electrolyte is higher than that predicted through Bruggeman's equation. Third, a higher value of the standard deviation for the solid phase as opposed to the liquid electrolyte indicates a wider range of values recorded in the current numerical simulations. This indicates the strong influence of the packing arrangement, and hence tortuosity, and a higher resistance to conduction of Li-ions and charge inside the solid, an aspect not captured by the empirical prediction of Eq. 13. While particle realization in Fig. 2a reveals a variation in concentration which is near uniform at each cross-section, Fig. 2b shows a larger pocket of solid which does not take part in the conduction process. As a
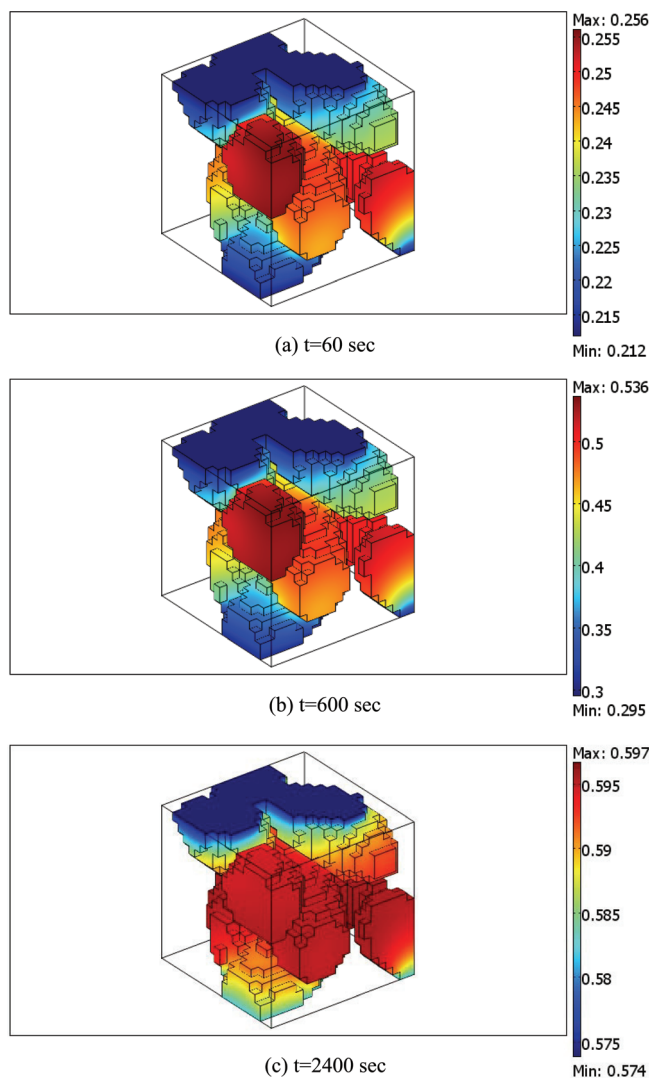
(a) t=60 sec

(b) t=600 sec

(c) t=2400 sec

Figure 9. (Color online) Solid state of charge (c_s/c_t) profiles at different time instants for 1C discharge rate.

(a) t=60 sec

(b) t=600 sec

(c) t=2400 sec

Figure 10. (Color online) Normalized reaction density (in A/m^2) at different time instants for 1C discharge rate.

result, the effective diffusivity for the latter is much lower compared to the former and indicates that using Bruggeman's equation in a macroscale simulation to characterize the packing of particles may not be accurate.

Surrogate based global sensitivity analysis reveals the dependence of normalized reaction density on the solid concentration and electric potential as well as the electrolyte electric potential. The difference between the total and main indices indicates the degree of cross-interaction between design variables. The volumetric reaction density, given by Eq. 14, can be regarded as a sum of j_{flux} at the particle-electrolyte interface, where j_{flux} is a function of local concentrations and overpotential (η). To gain an insight into the dependence of reaction density on $\overline{\overline{c}}_s$, $\overline{\varphi_s}$ and $\overline{\varphi_e}$, a separate surrogate-based analysis was performed to quantify the relative importance of $\overline{\overline{c}}_s$, $\overline{\varphi_s}$ and $\overline{\varphi_e}$ on the overpotential η. In the variable range given in Table IV, while $\overline{\varphi_s}$ and $\overline{\varphi_e}$ vary by ~1V, the maximum change in U_{OCP} due to variation in $\overline{\overline{c}}_s$ is 0.24V. Using kriging with the second-order regression model, and in the range given by $3.0V \le \overline{\varphi_s} \le 4.15V$, $-1.0V \le \overline{\varphi_e} \le 0V$ and $0.2 \le \overline{\overline{c}}_s \le 0.9$ with the constraint $-0.1 \le \overline{\varphi_s} - \overline{\varphi_e} - U_{OCP}\left(\overline{\overline{c}}_s\right) \le 0$, it was observed that the main effect of $\overline{\varphi_s}$ (main index = 0.55) and $\overline{\varphi_e}$ (main index = 0.42) dominated over that of $\overline{\overline{c}}_s$ (main index = 0.03), and the cross-interaction between variables was negligible ($<10^{-3}$). As a result, it can be expected that the
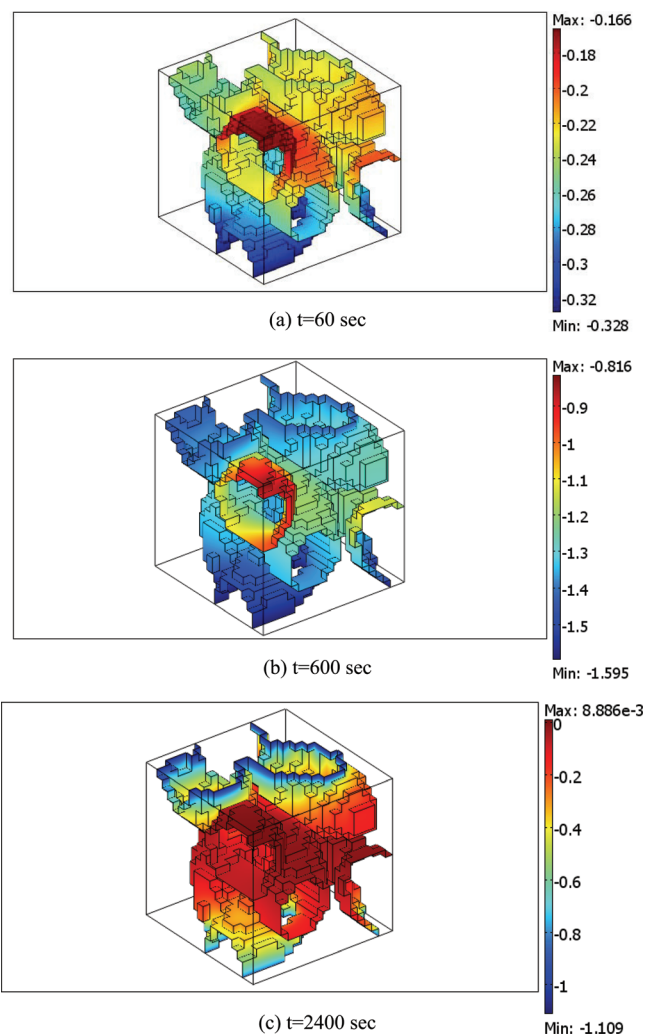
integrated reaction density will also show a negligible main effect due to solid concentration. As shown by the indices in Fig. 5, the main effect of solid concentration on the normalized reaction density is minimal, which corroborates the overpotential analysis. Moreover, for the normalized reaction density at the particle-electrolyte interface, the cross-interaction between variables dominates over the main effect. It should be noted that the current microscale analysis considers local variation in concentration and electric potential as boundary conditions for a more refined analysis, whereas pseudo-2D models use volume-averaged electric potential and electrolyte concentration in Eq. 16 to incorporate the reaction flux at the interface. Thus, it can be expected that using averaged values in Eq. 16, depending on the spatial variation in electric potential, together with a homogenized representation of the electrode, may lead to predictions inconsistent with a real system.

Normalized reaction density computed from micro- and macroscopic simulations reveals that the packing of solid in the REV had little effect, as microstructures corresponding to different effective transports yield similar results. As shown in Figs. 7 and 8, near the beginning of discharge for both rates, particle simulations indicate a Li-ion flux into the solid matrix higher than that predicted by the homogenous model. While the simulation results from the two methodologies are different during the course of discharge, the predictions are much more consistent near the end of the discharge cycle. To highlight the reasons for the wide temporal variation in reaction density, microscopic variation of concentration and flux at

three time instants corresponding to t = 60, 600, and 2400 s are examined here in greater detail. As shown in Fig. 9, near the initial stage of discharge corresponding to t = 60 s, the particle model indicates a narrow variation in the state of charge in the REV. From Fig. 10a it can be observed that the magnitude of normalized reaction density predicted by the microscopic simulations is highest at t = 600 s. As shown in Fig. 9, the state of charge variation in the solid phase is found to be wider at this time instant. At t = 2400 s the variation is again narrow.

As the normalized reaction density in the microscopic simulations is computed based on local distribution of flux at the particle-electrolyte interface, detailed analysis of the temporal variation of the former can be achieved by examining the latter at the particle scale. Figure 10 reveals two features of reaction density distribution at the microscale. First, the magnitude of local reaction density at t = 60 and 2400 s is predominantly lower that that for t = 600 s. Although the presence of high reaction density regions is noticed for t = 2400 s, these are fairly local and confined. As a result, the integrated reaction density at either t = 60 s or 2400 s is very different from that at t = 600 s. Second, as shown in Figs. 9 and 10, the magnitude of Li-ion flux into the solid is higher in regions where the state of charge is lowest. The open circuit potential of $LiMn_2O_4$ is related to the state of charge such that any increase in the latter results in a decrease in the former. Moreover, the flux at the particle-electrolyte interface depends on the concentration in the two phases and the surface overpotential given by Eq. 17. A closer inspection of the microscale results at t = 60 and 2400 s reveals that the overpotential varies between –0.01 to –0.005 V and –0.028 to 0.0002 V respectively. However, at t = 600 s the overpotential is much larger, and varies from –0.04 to –0.021 V. As a result, flux of Li-ions into the solid phase at this time instant can be expected to be the highest due to the higher magnitude of overpotential and explains the inconsistency in the prediction of reaction density using macro- and microscale simulations.

A discussion on the comparison of microscopic and pseudo-2D models is essential. In Figs. 7 and 8, the microstructures that are placed at different locations in the positive electrode are not correlated; i.e., the governing equations at each location are solved independently of other microstructures. Moreover, the microstructures are not coupled to the cell-level simulation. As a result, the summation of reaction density across the electrode may not be the same as the discharge rate, as the microscale and macroscale have not yet been coupled in the presented framework, which highlights the motivation behind the selection of surrogate based modeling to bridge the gap between these scales. Since the objective in this work is to accomplish the first stage of the multiscale model, we have quantified the impact of the electrode architecture on the microscale reaction density and transport properties and formulated reduced-order surrogate models for the same. In the future, we will present a complete framework by coupling these reduced-order models with a cell-level one-dimensional framework which will show that the summation of flux at any time instant across the electrode is a constant.

Conclusions

In this work, the electrochemical processes occurring at the particle-scale in the cathode of a Li-ion cell are analyzed through a multiscale modeling framework. Electrode microstructures constructed based on randomly packed ellipsoidal particles were simulated. As the discharge and electrochemical processes occur at different time and length scales, volume averaging is proposed as a tool to capture the physics on multiple scales.

Particle cluster simulations were used for the calculation of closure terms, such as effective transport properties and reaction density, which are introduced as part of the volume-averaging process. As the ratio of the effective to the bulk quantity remains the same irrespective of the transport property, only the results for the calculation of effective diffusivity for the solid and electrolyte are shown

in this work. A total of 24 random particle packings were used to compute the ratio of the effective and bulk diffusivity for both the solid and electrolyte phases. Through three-dimensional modeling of particle clusters it is shown that the calculated effective solid diffusivity could be much lower than that predicted using empirical relations such as the Bruggeman's equation. A higher value of the standard deviation for the solid phase also indicates the strong influence of packing, tortuosity and increased resistance to conduction inside the solid matrix, an aspect not captured by the Bruggeman's equation.

In addition to the calculation of effective transport, three-dimensional simulations using 24 different particle clusters in an REV were also conducted to capture the local variation of variables at the microscale using the boundary conditions based on a cell-level pseudo-2D simulation. Variables, namely the concentrations, electric potentials and their gradients were chosen for the construction of reduced-order surrogate models for the normalized reaction density. To achieve this, a rigorous procedure was followed that included (a) determining the ranges of variables in a cell-level simulation (based on a maximum possible discharge rate of 3C), (b) construction of design of experiments consisting of 387 sample points, (c) numerical experiments on these sample points, (d) formulation of reduced-order surrogate models, and (e) cross-validation. Of the different surrogate models trained on the DOE, a kriging model with second-order polynomial regression and Gaussian correlation was found to lead to the lowest prediction and PRESS errors.

Using this surrogate model, global sensitivity analysis was conducted to quantify the influence of solid and electrolyte concentration, electric potential and their gradients on the normalized reaction density. The main and total sensitivity indices for the electrolyte concentration and gradients of concentrations and potentials in both phases were found to be negligible, indicating the weak influence of these variables on the normalized reaction density. The cross-interaction between solid concentration, solid electric potential and electrolyte electric potential, quantified in terms of the difference between total and main indices, was found to dominate over the main effects in the reduced-order surrogate model for the normalized reaction density, indicating high correlation between variables.

Results from macroscopic and microscopic simulations were also compared. For microscopic simulations, different particle clusters were considered. It was shown that the packing of solid particles had little influence on the normalized reaction. However, particle simulations revealed a Li-ion flux different than that predicted by the porous-electrode model. The three-dimensional simulations show that the local variation of state of charge and overpotential leads to accumulation of Li-ions at selected regions in the REV, a phenomenon not captured by macroscopic formulations.

Thus, particle cluster simulations indicate the limitations associated with the use of empirical correlations in macroscale simulations, such as Bruggeman's equation, as these may under or overpredict the transport processes occurring inside a Li-ion cell. The present study offers a first-step towards integration of the effect of microstructure into a macroscale simulation through the calculation of effective transport and closure terms. These closure terms derived from the particle-cluster simulations could be incorporated into a macroscopic model to gain fast-prediction of battery performance. In future work, this analysis will be used to construct reduced-order models and ascertain variables that weakly influence battery performance, and thus greatly assist in eliminating variables so as to affect the experiments conducted on these energy systems.

Appendix A. Volume Averaging: Concepts and Theorems

Volume averaging relies on two averages, defined as the intrinsic ($\bar{\psi}_k^k$) and the superficial averaged ($\bar{\psi}_k$) quantities.[23–27] These identities are given as

$$\bar{\psi}_k^k = \frac{1}{dV_k} \int_{dV} \psi_k \gamma_k dV \qquad [\text{A-1}]$$

$$\bar{\psi}_k = \frac{1}{dV} \int_{dV} \psi_k \gamma_k dV \qquad [\text{A-2}]$$

where dV_k is the volume occupied by the phase k and γ_k is the phase function, given as

$$\gamma_k = \begin{cases} 1, & \text{in phase k} \\ 0, & \text{otherwise} \end{cases} \qquad [\text{A-3}]$$

The volume fraction ε_k is given by

$$\varepsilon_k = \frac{1}{dV} \int_{dV} \gamma_k(\vec{r}, t) dV \qquad [\text{A-4}]$$

The two averages are related through the volume fraction as

$$\bar{\psi}_k = \varepsilon_k \bar{\psi}_k^k \qquad [\text{A-5}]$$

In addition to these identities (Eqs. A1 and A2), volume averaging employs two theorems to simplify the averaging procedure when applied to partial differential equations that may involve spatial and temporal derivatives. Theorem 1 relates the average of the time derivative to the time derivative of the average,[23] and is given by

$$\frac{1}{dV} \int_{dV} \frac{\partial \psi_k}{\partial t} \gamma_k dV = \frac{\partial}{\partial t} \left[\frac{1}{dV} \int_{dV} \psi_k \gamma_k dV \right] - \frac{1}{dV} \int_{dA_k} \psi_k \vec{n} \cdot \vec{w} dA \qquad [\text{A-6}]$$

where dA_k is the interfacial area, $\vec{n}$ is the outward unit normal and $\vec{w}$ is the velocity of the microscopic interface. Theorem 2 relates the average of the spatial derivative to the spatial derivative of the average[23] as

$$\frac{1}{dV} \int_{dV} (\nabla \psi_k) \gamma_k dV = \nabla \left[\frac{1}{dV} \int_{dV} \psi_k \gamma_k dV \right] + \frac{1}{dV} \int_{dA_k} \psi_k \vec{n} dA \qquad [\text{A-7}]$$

Appendix B. Surrogate Models

Polynomial response surface.— In this model, function of interest f is approximated as a linear combination of polynomial functions of design variables $\mathbf{x}$ (Refs. 29,34,35)

$$f(\mathbf{x}) = \sum_j \beta_j a_j(\mathbf{x}) + \varepsilon \qquad [\text{B-1}]$$

where β_j is estimated through a least-squares method so as to minimize the variance, $a_j(\mathbf{x})$ are basis functions, and the errors ε have an expected value equal to zero.

Kriging (KRG).— The kriging model estimates the objective function as a sum of two components: a polynomial regression trend (h) and a high frequency variation (Z).[29,35] Thus, the objective function is approximated as

$$f(\mathbf{x}) = \sum_j \beta_j h_j(\mathbf{x}) + Z(\mathbf{x}) \qquad [\text{B-2}]$$

The departure function $Z(\mathbf{x})$ is correlated based on the distance between sampling locations. Commonly used formulations for the departure function include Gaussian, exponential, linear, cubic and spline functions.

Radial basis neural network (RBNN).— In this model, the objective function is approximated as a linear combination of N_{RBF} radially symmetric basis functions ($g_j(\mathbf{x})$) and coefficients w_j (Refs. 29,35) as

$$f(\mathbf{x}) = \sum_{j=1}^{N_{RBF}} w_j g_j(\mathbf{x}) \qquad [\text{B-3}]$$

Weighted-average surrogate (WAS) model.— In addition to individual surrogate models, a weighted averaging concept that is based on combining different surrogates for a more robust approximation[36] can also be utilized. A weighted average surrogate model can be written as

$$f_{WAS}(\mathbf{x}) = \sum_{i=1}^{N_{SM}} w_i(\mathbf{x}) f_i(\mathbf{x}) \qquad [\text{B-4}]$$

where N_{SM} is the number of surrogate models, $f_{WAS}(\mathbf{x})$ is the predicted response by the weighted average model, $f_i(\mathbf{x})$ is the predicted response from the ith surrogate model, and $w_i(\mathbf{x})$ is the weight associated with the ith surrogate model at design point $\mathbf{x}$ (such that $\sum_{i=1}^{N_{SM}} w_i(\mathbf{x}) = 1$).[36]

List of Symbols

a_s	interfacial area per unit volume
c_e	Li-ion concentration in the electrolyte
$\overline{c_e}$	volume-averaged Li-ion concentration in the electrolyte
c_s	Li-ion concentration in the solid
$\tilde{c}_s$	fractional Li-ion concentration in the solid
$\bar{c}_s$	volume-averaged solid concentration
c_t	maximum stoichiometric concentration
dA_s	interfacial area element
dV	volume element
D_e	diffusivity in the electrolyte phase
D_e^{eff}	effective diffusivity in the electrolyte phase
D_s	diffusivity in the solid phase
D_s^{eff}	effective diffusivity in the solid phase
$D_{s,n}$	solid diffusion coefficient of the negative electrode
$D_{s,p}$	solid diffusion coefficient of the positive electrode
f	mean molar activity coefficient
F	Faraday's constant
j_{flux}	normalized reaction flux density
J_{C_s}	volumetric reaction density
k	rate of reaction
$\vec{n}$	normal vector
$\vec{r}$	position vector
R	universal gas constant
$R_{s,n}$	particle radius in negative electrode
$R_{s,p}$	particle radius in positive electrode
t	Time
t_+^0	Cation transference number
T	Temperature
U_{OCP}	open circuit potential
V	Volume
$\vec{w}$	interface velocity
z	Coordinate

Greek

α	Bruggeman's exponent
δ_n	thickness of negative electrode
δ_p	thickness of positive electrode
δ_s	thickness of separator
ε_n	volume fraction of solid in negative electrode
ε_s	volume fraction of solid
φ_e	electric potential in the electrolyte
$\overline{\varphi_e}$	volume-averaged electric potential in the electrolyte
φ_s	electric potential in the solid
$\overline{\varphi_s}$	volume-averaged solid electric potential
γ_s	solid phase function
η	overpotential
κ	ionic conductivity of the electrolyte
κ^{eff}	effective ionic conductivity of the electrolyte
σ	electronic conductivity of the solid
σ^{eff}	effective electronic conductivity of the solid

References

1. M. Endo, C. Kim, K. Nishimura, T. Fujino, and K. Miyashita, *Carbon*, **38**, 183 (2000).
2. M. D. Levi and D. Aurbach, *J. Phys. Chem. B*, **101**, 4641 (1997).
3. M. Doyle, J. Newman, A. S. Gozdz, C. M. Schmutz, and J. M. Tarascon, *J. Electrochem. Soc.*, **143**, 1890 (1996).
4. J. L. Shui, G. S. Jiang, S. Xie, and C. H. Chen, *Electrochim. Acta*, **49**, 2209 (2004).
5. R. Yazami and Y. Ozawa, *J. Power Sources*, **153**, 251 (2006).

6. P. Arora, M. Doyle, A. S. Gozdz, R. E. White, and J. Newman, *J. Power Sources*, **88**, 219 (2000).
7. M. W. Verbrugge and R. S. Conell, *J. Electrochem. Soc.*, **149**, A45 (2002).
8. B. Y. Liaw, G. Nagasubramanian, R. G. Jungst, and D. H. Doughty, *Solid State Ionics*, **175**, 835 (2004).
9. B. Haran, B. N. Popov, and R. E. White, *J. Power Sources*, **75**, 56 (1998).
10. S. Santhanagopalan, Q. Guo, and R. E. White, *J. Electrochem. Soc.*, **154**, A198 (2007).
11. M. Doyle, T. F. Fuller, and J. Newman, *J. Electrochem. Soc.*, **140**, 1526 (1993).
12. T. F. Fuller, M. Doyle, and J. Newman, *J. Electrochem. Soc.*, **141**, 1 (1994).
13. W. Du, A. Gupta, X. Zhang, A. M. Sastry, and W. Shyy, *Int. J. Heat Mass Transfer*, **53**, 3552 (2010).
14. P. Ramadass, B. Haran, R. E. White, and B. N. Popov, *J. Power Sources*, **123**, 230 (2003).
15. Y.-H. Chen, C. W. Wang, G. Liu, X.-Y. Song, V. S. Battaglia, and A. M. Sastry, *J. Electrochem. Soc.*, **154**, A978 (2007).
16. X. Zhang, W. Shyy, and A. M. Sastry, *J. Electrochem. Soc.*, **154**, A910 (2007).
17. X. Zhang, A. M. Sastry, and W. Shyy, *J. Electrochem. Soc.*, **155**, A542 (2008).
18. R. E. Garcia, Y.-M. Chiang, W. C. Carter, P. Limthongkul, and C. M. Bishop, *J. Electrochem. Soc.*, **152**, A255 (2005).
19. C.-W. Wang and A. M. Sastry, *J. Electrochem. Soc.*, **154**, A1035 (2007).
20. M. Smith, R. E. Garcia, and Q. C. Horn, *J. Electrochem. Soc.*, **156**, A896 (2009).
21. R. E. Garcia and Y.-M. Chiang, *J. Electrochem. Soc.*, **154**, A856 (2007).
22. X. Zhang, Ph.D., Dissertation, University of Michigan (2009).
23. W. Shyy, S. S. Thakur, H. Ouyang, J. Liu, and E. Blosche, *Computational Techniques for Complex Transport Phenomena*, Cambridge University, New York (2005).
24. C. Y. Wang, W. B. Gu, and B. Y. Liaw, *J. Electrochem. Soc.*, **145**, 3407 (1998).
25. P. D. Vidts and R. E. White, *J. Electrochem. Soc.*, **144**, 1343 (1997).
26. W. G. Gray, *Chem. Eng. Sci.*, **30**, 229 (1975).
27. E. Sozer and W. Shyy, *Int. J. Numer. Methods Heat Fluid Flow*, **18**, 883 (2008).
28. K. K. Patel, K. M. Paulser, and J. Desilvestro, *J. Power Sources*, **122**, 144 (2003).
29. N. V. Queipo, R. T. Haftka, W. Shyy, T. Goel, R. Vaidyanathan, and P. K. Tucker, *Prog. Aerosp. Sci.*, **41**, 1 (2005).
30. A. Donev, S. Torquato, and F. H. Stillinger, *J. Comp. Phys.*, **202**, 737 (2005).
31. S. J. Hollister and N. Kikuchi, *Biotechnol. Bioeng.*, **43**, 586s (1994).
32. N. Tsafnat, G. Tsafnat, and A. S. Jones, *Fuel*, **87**, 2983 (2008).
33. Y. Saad, *Iterative Methods for Sparse Linear Systems*, Society for Industrial and Applied Mathematics, Philadelphia, PA (2003).
34. Y. Mack, T. Goel, W. Shyy, and R. T. Haftka, *Stud. Comp. Intel.*, **51**, 323 (2007).
35. T. Goel, D. J. Dorney, R. T. Haftka, and W. Shyy, *Comput. Fluids*, **37**, 705 (2008).
36. T. Goel, R. T. Haftka, W. Shyy, and N. V. Queipo, *Struct. Multidiscip. Optim.*, **33**, 199 (2007).